Nano-CT measurement of pore-fracture evolution and diffusion transport induced by fracturing in medium-high rank coal

Qifeng Jia [a,b,c], Dameng Liu [a,b,*], Yidong Cai [a,b], Yuejian Lu [a,b,c], Rui Li [c], Hao Wu [a,b], Yingfang Zhou[c,d]

[a] *School of Energy Resources, China University of Geosciences, Beijing 100083, China*

[b] *Coal Reservoir Laboratory of National Engineering Research Center of CBM Development & Utilization, China University of Geosciences, Beijing 100083, China*

[c] *School of Engineering, Fraser Noble Building, King's College, University of Aberdeen, AB24 3UE Aberdeen, UK*

[d] *Department of Energy Resources, University of Stavanger, Stavanger, 4021, Norway*

* Corresponding author at: School of Energy Resources, China University of Geosciences, Beijing 100083, China.

E-mail address: dmliu@cugb.edu.cn (D. Liu), Tel: +86-10-82323971; fax: + 86-10-82326850.

Abstract

Fracturing, as a common fracture-making technique, can improve the permeability of coal seams to enhance fluid transport efficiency. To quantitatively evaluate the microscopic characteristics of medium-high rank coal, the loaded pore-fracture system was characterized by computerized tomography (CT) scanning under triaxial loading, followed by the analysis of stress-strain evolution, stress sensitivity and three-dimensional (3D) fractal dimension. Combined with snow algorithm and incompressible steady laminar flow simulation, the heterogeneous distribution of fluid pressure is investigated, focusing on the diffusion effect of gas transport. The results

show that the strain of the high-rank coal Chengzhuang (CZ) in the linear elastic stage increases from 0.25% to 1.25%, greater than that of the medium-rank coal Qiyi (QY) from 0.75% to 1.63%, demonstrating a slight lag of the high-rank coal from the linear elastic stage into the yielding stage. The porosity of CZ changes from 1.66% to 13.58% and that of QY varies from 1.74% to 22.28% after fracturing, reflecting that the primary and secondary pores of the medium- and high-rank coals form a complex network structure for fluid transport through continuous connection-expansion. When the strain is between 0.75% and 1.25%, the stress sensitivity coefficient of CZ decreases from 0.13 to 0.02. Moreover, there are many mutation points in the 3D fractal dimension of coal samples after fracturing, mainly due to the generation of new pore-fractures at different locations of the computational domain. For fluid transport, the pressure of QY after fracturing spreads in a wider range than CZ, accompanied by more distribution of high fluid pressure. The diffusion coefficient of the fractured CZ is 350 times higher than that of the original coal under the gas pressure condition of 0.5 MPa, which provides the possibility for more gas to be converted from Knudsen diffusion to transition diffusion or Fick diffusion in the channel.

Keywords: Nano-CT; Fracturing; Strain; Pore; Fluid flow; Diffusion transport

1. Introduction

Efficient exploitation of coalbed methane (CBM) has become one of the essential measures to tackle the increasing concerns over natural gas scarcity to enhance energy security (Connell, 2009; Dai et al., 2021; Lu et al., 2022a). CBM is an unconventional natural gas generated from organic material in the process of physicochemical and

biological interaction (Tamamura et al., 2020). As a source rock or storage carrier, the pore system in coal reservoirs features multi-scale, micro-scale fracture and sub-micron pore in matrix, as well as large specific surface area (Li et al., 2021a; Ribeiro et al., 2022; Wang et al., 2016; Xu et al., 2022).

Many testing techniques, including scanning electron microscopy (SEM), nuclear magnetic resonance (NMR), micro-scale computation tomography (CT) scan, atomic force microscopy (AFM), and focused-ion beam-scanning electron microscopy (FIB-SEM), have been used to characterize pore-fractures in coal (Shi et al., 2020; Wang et al., 2020b; Yu et al., 2020; Zhao et al., 2018). For example, with the support of SEM measurement, Chen et al. (2021a) claimed that the development direction of natural fracture in coal at macroscopic scale was parallel to that at the fine scale; they also proposed two fracture development models, synchronous development of dense grids and the main fractures with loose distribution first and then mutual interpenetration, respectively. It is also noticed that the estimated formation properties, e.g., porosity, permeability, movable fluid saturation and bound fluid saturation, from NMR are strongly affected by the selected T_2 cutoff value (Zhao et al., 2021c). With the support of micro-CT imaging, Wang et al. (2021a) concluded that the fracture volume, density, connectivity, and fracture rate in coal samples underwent three stages of deformation, slow decrease, slow increase and sharp increase under triaxial loading. Li et al. (2020d) obtained quantitative information on Young's modulus and adhesion force of coal samples by AFM, indicating that adhesion reflecting surface energy information was affected by surface topography. The mechanical properties of matrix and minerals in

coal differ significantly, so the influence of mineral distribution should be carefully considered during fracturing. Li et al. (2020a) conducted a FIB-SEM study of pore structure in coal, and they suggested that there may be nonmonotonic correlation between porosity and fractal dimension due to the complexity of pore structure and mineral filling. Moreover, different forms of fluid geology occur throughout the process of CBM formation, evolution, enrichment, accumulation and production, which in turn affect the physicochemical properties of the pore-fractures (Du et al., 2020; Liu et al., 2018; Zhao et al., 2021b).

The development degree and spatial distribution of pore-fracture in coal reservoirs determine the fluid diffusion and seepage capacity, and thus influence the transport process in CBM (Roslin et al., 2020; Zhao et al., 2018). In fact, both types of kinetic mechanisms often occur simultaneously and act together with the change of geological conditions during CBM accumulation (Liu et al., 2021a; Tao et al., 2020). Generally speaking, the single-pore model is suitable for studying the diffusion behavior of methane in bright coals, while the double-pore model is applicable to dull coals with complex pore-fracture structures (Liu et al., 2022c; Zhang et al., 2021). Besides, fluid activity affects the material evolution and energy distribution in coal reservoirs throughout the coal-forming process, including sedimentation, metamorphism, magmatic and tectonic activity (Connell, 2009; Fu et al., 2021; Hou et al., 2022; Melnichenko et al., 2009).

As shown in the literature, there are previous works that characterize the pore-fracture evolution on the micron scale or static physical structure (Chen et al., 2019;

Kang et al., 2019; Tan et al., 2019; Zheng et al., 2018). Interestingly, the changes in thermal expansion during methane adsorption by pores in coal were evaluated quantitatively (Chen et al., 2021b; Kang et al., 2022; Zheng et al., 2019), which provided new ideas for a comprehensive understanding of adsorption effects (Jia et al., 2022b; Liu et al., 2022b; Xie et al., 2022). However, the evolution of pore-fracture dynamics at the nano-scale after fracturing has rarely been investigated. This study analyzed the pore-fracture variations of medium-high rank coal during loading by nano-CT with full consideration of stress sensitivity. According to the characteristics of spatial fluid transport (Jia et al., 2020; Liu et al., 2022a), the heterogeneous distribution of pore-fractures was characterized. Combined with the 3D fractal dimension and fluid pressure change, the diffusion effect of CBM enrichment production was revealed. These works have been rarely reported in previous studies.

In this paper, the pore-fracture evolution and its influence on fluid flow in medium-high rank coal were quantified using nano-CT scanning; this was accomplished by first imaging the pore system of coal under triaxial loading, and then pore-fracture system was quantified at different scales. Subsequently, the variation of the 3D fractal features with the computational domain was characterized by the box-counting. To study the fluid transport behavior throughout the fracturing process, pressure distribution was evaluated by combining incompressible steady laminar flow simulation and CBM diffusion experiment. The research results provide contribution to the fine quantification of the dynamics variation of the transport medium at the micron scale in the coal reservoir.

2. Sample preparation and measurements

2.1. Coal sampling and basic analysis

The coal samples, with original dimensions of about 500×300×300 mm, were collected from Chengzhuang (CZ) and Qiyi (QY) coal mines in Qinshui Basin. The coal samples were packed with waterproof and shockproof protective foam at the field and then immediately sent to the laboratory for fundamental parameters measurements. According to the international standards of ISO 7404.3–1994 and ISO 7404.5–1994 (Li et al., 2021a; Zhou et al., 2020), the maximum vitrinite reflectance, $R_{o,\,max}$, of the coal samples were measured by a Leitz MPV-III microscope photometer and industrial components were determined by the automatic industrial analyzer SDLA618. As shown in Table 1, the $R_{o,\,max}$ of the two coal samples are 2.84% and 1.85%, respectively, indicating that there is a wide range of microfracture developed in the selected coal samples (Dai et al., 2020b; Roslin et al., 2020). Besides, CZ belongs to high-rank coal, and QY corresponds to medium-rank coal. The industrial components differ, with ash content of 18.21% and 9.91% and volatile content of 6.31% and 13.58%, respectively. To ensure accurate testing of the experiments, the coal cores were taken by a vertical drilling machine and subsequently ground on a horizontal surface grinder, allowing the final coal samples to be machined into columns with a diameter of 2.5 mm and a height of 5 mm. Afterward, the coal column was treated by high-pressure freezing and subsequent freeze-drying in the same way as (Keller et al., 2013), thus minimizing the evolution of the coal column during the whole process.

Table 1 Sample information and basic parameters of the selected coals.

Samples	$R_{o,max}$ (%)	Per (mD)	Proximate analysis (%)				Coal maceral composition (%)	
			M_{ad}	A_{ad}	V_{ad}	FC_{ad}	V	I
CZ	2.84	0.02	0.54	18.21	6.31	74.94	94.7	5.3
CZ-1	2.80	0.03	0.58	17.98	6.25	75.19	94.5	5.5
CZ-2	2.88	0.02	0.53	18.42	6.36	74.69	94.6	5.4
QY	1.85	0.09	1.27	9.91	13.58	75.24	93.1	6.9
QY-1	1.84	0.09	1.33	9.89	14.01	74.77	93.4	6.6
QY-2	1.86	0.08	1.28	9.93	13.49	75.30	92.9	7.1

Note: $R_{o,max}$, maximum vitrinite reflectance; Per, permeability; M_{ad}, moisture (air-dried basis); A_{ad}, ash (air-dried); V_{ad}, volatile matter (dry, ash-free basis); FC_{ad}, Fixed carbon (air-dried basis); V, vitrinite; I, inertinite.

2.2. Nano-CT measurements under triaxial loading

In this work, the phoenix nanotom m nano-CT scanner was equipped with a triaxial loading experimental system to image the coal sample (see Fig. 1a). The nano-CT scanning system consists of an X-ray source, array detector, turntable and data processing module (see Fig. 1b and c). The scanner works by transmitting beams of X-ray photons through the volume of the coal samples and unto a detector. The intensity values of the transmitted beams are then used to construct a 3D grayscale image of the sample. Since coal contains matrix, clay, mineral and sporophyte with different densities, there are differences in the degree of X-ray absorption or scattering by these substances themselves, making a significant difference in the attenuation of emitted photons reaching the detector (Akhondzadeh et al., 2020; Wang et al., 2020a). This, in turn, produces different electron cloud density distribution maps.

The scanning device is derived from a temperature self-stabilized digital GE DXR detector (3072×2400 pixels) with a spatial resolution of 800 nm, enabling the detection of nano details. Before placing the sample, we ensured the highest resolution under the

volume of coal sample by adjusting the triaxial position so that the sample was directly in the middle of the X-ray (Roslin et al., 2020). Afterwards, to ensure the scanning accuracy, the detector was calibrated after fixing the sample, i.e., the window was observed for the presence of uniform snowflake images (Akhondzadeh et al., 2020; Keller et al., 2013; Zhao et al., 2018). The equipment started scanning at a voltage of 160 kV and a current of 120 μA. After rotating coal sample on the turntable by 360°, the nano-CT scan allowed us to obtain a collection of images at different angles, which represented the electron density distribution in the whole 3D space of coal sample. These electron cloud distribution images were then used to construct 3D data volumes with pore-fracture using software AVIZO and VGSTUDIO.

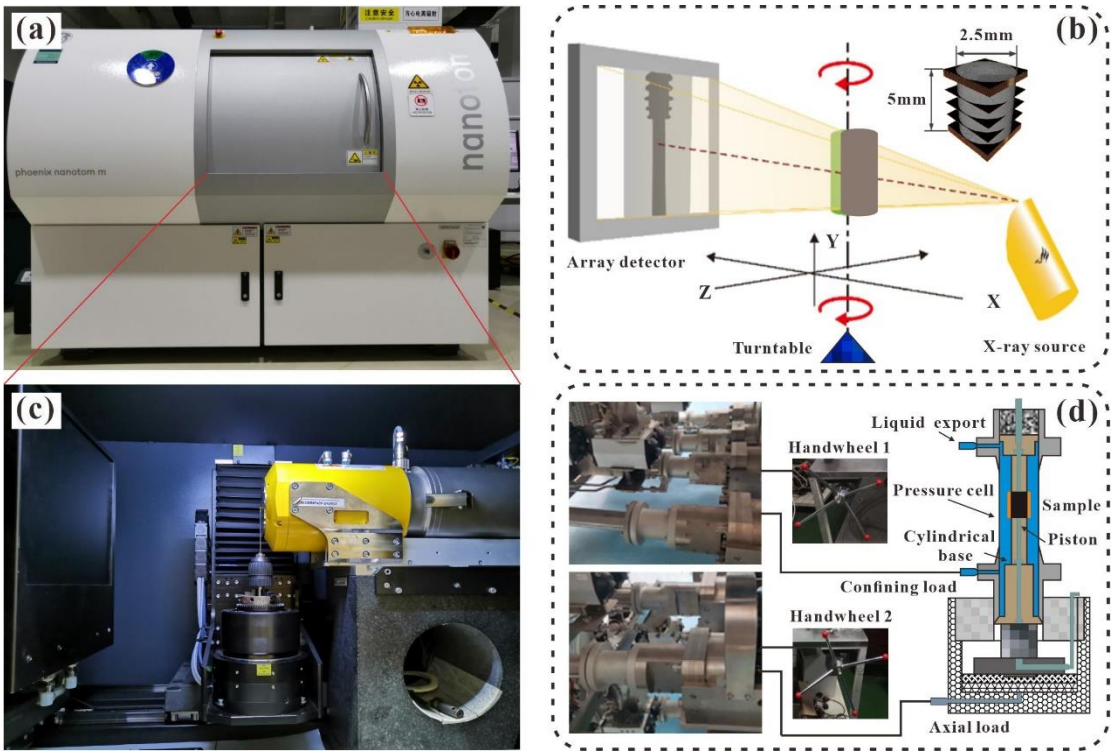

Fig. 1. Nano-CT scanning experimental device under triaxial loading. (a) Industrial nano-CT scanning experimental instruments; (b) Schematic diagram of scanning principle; (c) Internal structure of nano-CT; (d) Triaxial loading system.

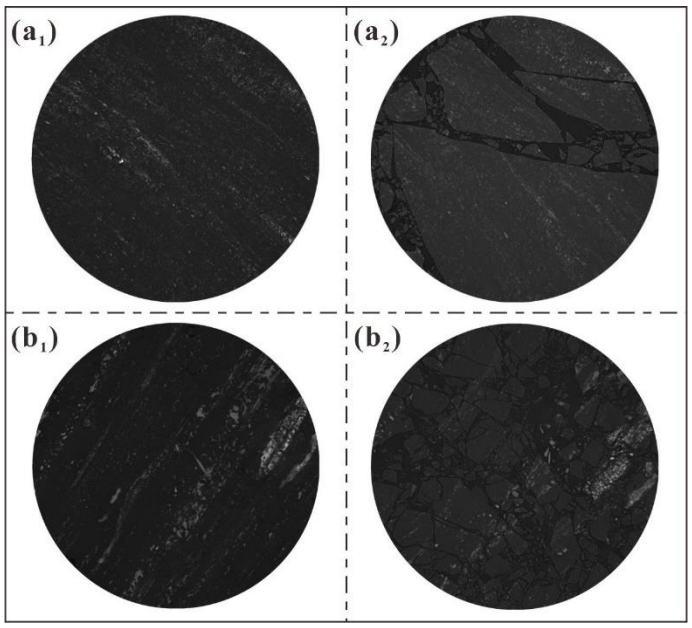

Fig. 2. Comparison of medium- and high-rank coals before and after fracturing. a_1 and a_2 indicate the high-rank coal sample CZ before and after fracturing, respectively; b_1 and b_2 show the medium-rank coal sample QY before and after fracturing, respectively.

2.3. Fracturing procedures

In order to analyze the mechanical properties of coal samples under different pressures, we used handwheel rotation to control the axial displacement to apply pressure (Li et al., 2020a; Shi et al., 2020). The prepared coal samples were fixed between two pistons using tweezers and then mounted in a triaxial pressure cell fixed on a cylindrical base. Subsequently, the confining pressure chamber of the gripper was judged to be filled with water by observing the transparent tubes, followed by applying the confining pressure and axial pressure with rotating handwheels. To prevent the clarity and sealing effect from being affected by the shaking of coal sample during triaxial loading, a support force of 5 N was applied to coal sample before loading pressure. During the whole scanning process, the confining pressure was at 1.2 MPa,

and the axial pressure increased from 0 MPa until coal sample was broken. As shown in Fig. 2, many fractures can be observed in the medium- and high-rank coals fractured using the device in Fig 1d, which is very beneficial for fluid transport during drainage of CBM wells. The fractured CZ generated several intersecting fractures that changed the distribution of some of the original minerals. In particular, the fractured QY generated many connected fractures from the middle to the edge. As a result, the efficiency of methane transport is significantly increased.

3. Determination of pore network and fluid transport

3.1. Image processing programs

In the micrographs of coal samples, reasonable threshold segmentation facilitates the extraction of coal matrix and mineral boundaries (Shi et al., 2020; Zhao et al., 2018). To obtain the topology of the pore-fracture network, this paper adopts the method of Zhang et al. (2022) to process the scanned CT images. The minimum equivalent diameter of the 3D pore network was determined to be in the range of 320 to 480 μm, and the size of the volume pixel was in the range of 0.8–0.85 μm. Since the images of CT scans contain noise that may affect the accuracy of subsequent data analysis, noise reduction is an essential step for calculating the fractal dimension. The 1200 CT images were changed from 16 to 8 bits using the software Image J, followed by processing a selected region of 1200 × 1200 voxels by the median filtering so that the number of isolated noise points was significantly reduced. Subsequently, the critical value of threshold segmentation was calculated by Otsu's algorithm, while the accuracy was

verified using the pore size distribution obtained from the mercury injection experiment. After that, a typical 500×500×500μm cube was selected from the middle of the whole coal column, and the pore throat network was extracted by the maximum ball algorithm (Fig. 3).

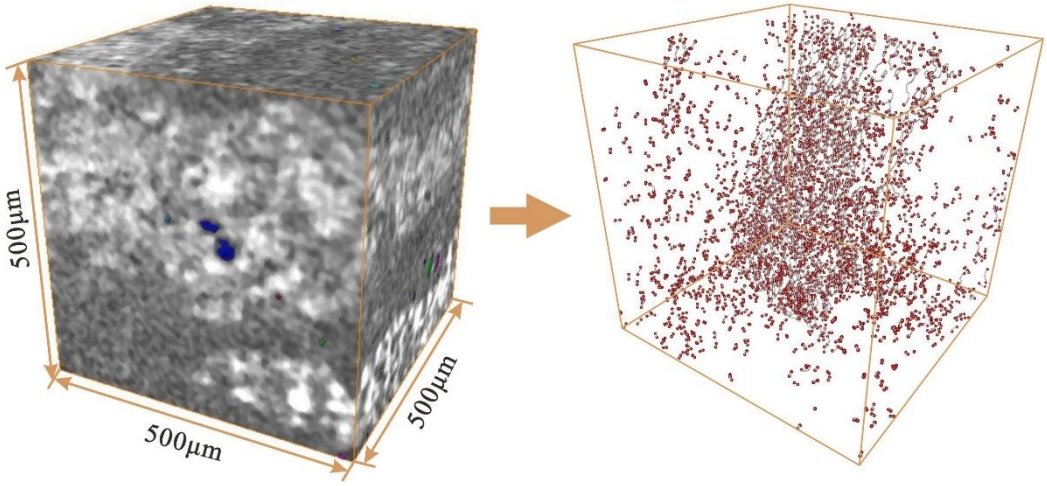

Fig. 3. Extracted pore network model.

3.2. Fractal calculation

As an essential parameter to describe the complexity and irregularity of porous media, the fractal dimension has been widely used by scholars (Mishra et al., 2018; Qin et al., 2020; Wu et al., 2019b). The 2D and 3D fractal dimensions of CT images can be calculated by the box-counting, thus becoming one of the popular methods (Mangi et al., 2020). We computed the fractal dimension of 1200 CT images (Wu et al., 2019a; Zhao et al., 2021a), and the process consists of three steps: (i) cropping these samples into 9 cubes with different growth states, meaning that a new cube was generated every 10 pixels until the side length reached the original sample length; (ii) choosing the side length r of the square boxes (or cubes for 3D) from the divisors used to cover the length and width of the binary image, followed by calculating the number of boxes N(r) with

pore pixels greater than 1; (iii) using linear correlation to match log N(r) and log (r), whose slope indicated the 2D or 3D fractal dimension.

3.3. Flow simulation in the pore-scale

The boundary conditions of inlet pressure of 2.5 MPa and outlet pressure of 0.1 MPa were set according to the actual bottom flow pressure in CBM well drainage. Subsequently, the fluid pressure distribution after fracturing the medium-high rank coal was simulated by combining snow algorithm and incompressible steady laminar flow. The pressure control equation is as follows:

$$\sum_{j=0}^{N} Q_{ij} = \sum_{j=0}^{N} K_{ij}(P_i - P_j) = 0 \quad (1)$$

$$K_{ij} = \frac{\pi}{8\mu l_{ij}}(r_{ij})^4 \quad (2)$$

Where *i* and *j* represent the pores connected at both ends of the throat; *Q* denotes the flow rate. *K* reflects the hydraulic conduction coefficient; *Pi* and *Pj* represent the pressure of the *i*th pore and the *j*th pore, respectively. μ is the dynamic viscosity of the liquid; *l* and *r* represent the length and radius of the throat, respectively.

3.4. Diffusion testing

To clarify the change of gas diffusion after fracturing of medium- and high-rank coals, a CBM diffusion coefficient tester was used to test the methane diffusion changes under triaxial loading. The test instrument consists of core gripper, pipe valve, gas cylinder, confining pressure pump, thermostat box, equilibrium chamber, gas chromatography system, pressure system, vacuum system and data acquisition system.

Firstly, the prepared coal column was dried and evacuated to remove water and residual gas from the internal pores, and then put into the core gripper, followed by the injection of methane gas into gas chamber 1 and nitrogen gas into gas chamber 2 under different gas pressure to adjust the two sealing chambers and balance the pressure. Afterward, the concentrations of methane and nitrogen were measured as the initial concentrations using a meteorological chromatography system. The concentrations of methane and nitrogen in the two gas chambers were determined again after 48 h, respectively (Liu et al., 2020; Song et al., 2022; Wang et al., 2021b; Xu et al., 2015). Finally, the results of the two measurements were substituted into the following equation to calculate the CBM diffusion coefficient D:

$$D = \frac{\ln \frac{C_{CH_4} - C_{N_2}}{C'_{CH_4} - C'_{N_2}}}{Bt} \quad (3)$$

where:

$$B = \frac{S}{L}\left(\frac{1}{V'} + \frac{1}{V''}\right) \quad (4)$$

where S is the cross-sectional area of coal sample and L is the height of sample. t denotes the diffusion time. V' and V'' are the volumes of gas chambers 1 and 2, respectively.

4. Results and discussion

4.1. Evolution of stress and strain during fracturing

To better demonstrate the mechanical properties during the fracturing process, the stress-strain curves of the medium- and high-rank coals are shown in Fig. 4. The fracturing process of both coals can be divided into the initial compression stage, linear

elastic stage, yielding stage, peak damage stage and residual stage. With the increase of axial stress, the fractures of two kinds of coal samples experience the damage phenomena of compaction, growth, and penetration (Duan et al., 2021; Li et al., 2020a). In the initial compression stage, the two curves are concave, indicating that the rate of stress change increases more than the strain. It is noteworthy that the maximum stress of 10 MPa for the medium-rank coal QY at this stage is much larger than that of 5.7 MPa for the high-rank coal CZ, implying that QY possesses more developed natural fractures (Wang et al., 2021a). As the axial stress continues to be loaded, CZ preferentially enters the linear elastic stage. Some new microfractures appear on the surface of the matrix, which is due to the damage to the coal body caused by the continuous accumulation of energy (Ju et al., 2021). Although the new fractures increase, they do not offset the volume reduction caused by the compression effect in the early stage, which is similar to the study of (Wang et al., 2021a). At this stage, the strain of CZ increases from 0.25% to 1.25%, greater than that of QY from 0.75% to 1.63%, demonstrating a slight lag of the high-rank coal from the linear elastic stage into the yielding stage. The presence of the confining pressure increases the stress on the pore-fracture surface, which inhibits the slip deformation after axial pressure loading, resulting in an increase in the ultimate strength of coal samples. When the stress reaches 11.5 MPa, the CZ enters the peak damage stage. At the moment, the generation, crossover and penetration of a large number of macroscopic fractures promote the transport of fluid in the coal samples.

As depicted in Fig. 2, for both coal samples, the mineral development affects the

pore-fracture penetration after fracturing. It should be noted that the stress of 16.8 MPa of QY is greater than that of 11.5 MPa of CZ when the ultimate peak is reached, showing that the compressive strength of the medium-rank coal is greater than that of the high-rank coal. Subsequently, the deformation of the two coal samples in the residual stage is extremely unstable, and the sedimentary divergence may occur in the actual stratum (Deschamps et al., 2017; Xie et al., 2020). In the whole process, the presence of strip minerals makes the fracture network more complex after fracturing. However, the total volume of fractures in coal tends to decrease first and then increase.

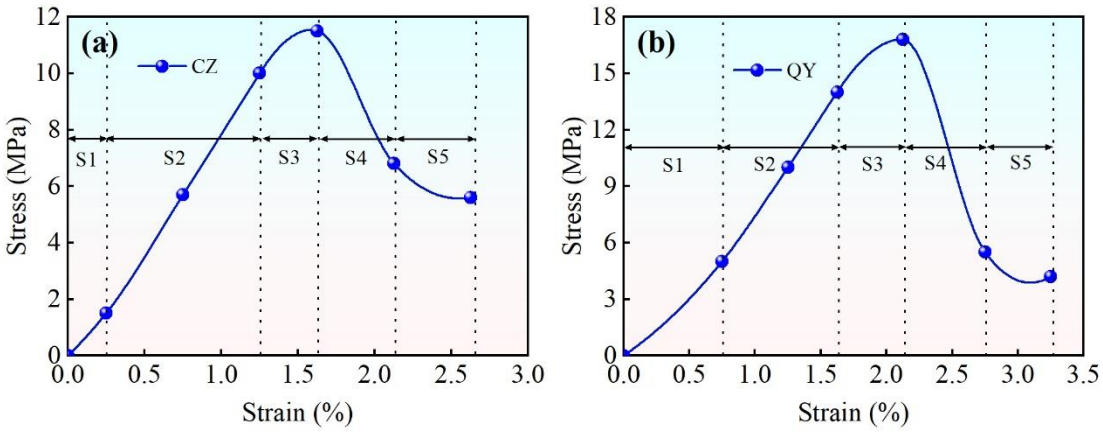

Fig. 4. Stress-strain variation curves during fracturing of medium- and high-rank coals. S1, S2, S3, S4 and S5 denote the initial compression stage, linear elastic stage, yielding stage, peak damage stage and residual stage, respectively.

4.2. Dynamic change of the loaded pore-fracture system

4.2.1. Microscopic variation characteristics of pore-fracture

Studying the changes in the loaded pore-fracture system can contribute insight into the fluid transport in coal reservoirs (Dai et al., 2020a; Li et al., 2020a; Zhou et al., 2018). According to the development characteristics of the actual coal seams in Qinshui

Basin, the classification criteria of pore-fractures proposed by Cai et al. (2013) are adopted in this paper. That is, the pore-fractures in coal are divided into super-micropores (< 2 nm), micropores (2-10 nm), mesopores (10-10^2 nm), macropores (10^2-10^3 nm), super-pores (10^3-10^4 nm) and microfractures (> 10^4 nm). As illustrated in Fig. 5, the overall porosity of the two coal samples changes significantly after fracturing, where CZ increases from 1.66% to 13.58% (Fig. 5a_1 and a_2), indicating that the resistance to fluid transport in the channel is significantly reduced. For the coal sample QY, the porosity changes from 1.74% to 22.28% after fracturing (Fig. 5b_1 and b_2). Some obvious pore-fracture network connections can be observed, which may provide a strong condition for the conversion of methane in coal from Knudsen diffusion to Fick diffusion (Lu et al., 2020). Before fracturing, some narrow microfracture channels can be found in QY, while almost invisible in CZ, implying that the original reservoir in QY is more favorable for fluid transport and accumulation. During the whole fracturing process, the change of porosity is divided into four stages: (i) the overall porosity decreases due to compression; (ii) under the action of stress, the pores at the edge of coal sample expand to form large pores and fractures which increases the porosity; (iii) the destruction of the originally strong crystallization and cementation among mineral particles leads to the generation of new pores; (iv) the pore-fracture penetration between the middle and the edge of coal sample causes a significant increase in porosity.

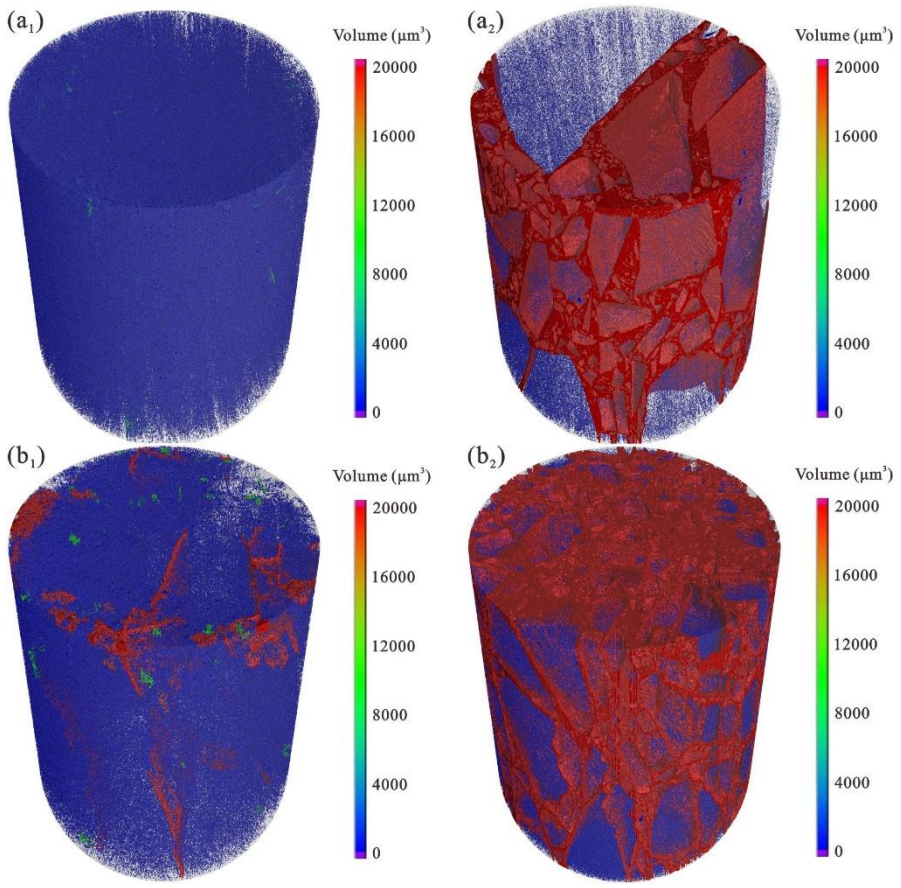

Fig. 5. 3D models of pore-fracture distribution of different coal samples. a_1 and a_2 are the original and fractured models of high-rank coal CZ, respectively; b_1 and b_2 are the original and fractured models of medium-rank coal QY, respectively.

To further clarify the pore size change law of medium- and high-rank coals, the pore size distribution of CZ and QY after fracturing is shown in Fig. 6. For the high-rank coal CZ, the super-large pores with pore diameter from 1 to 10 μm in the original state dominate, accounting for 71%, which provides favorable conditions for the pore-fracture connectivity after fracturing. Within the observed range of spatial resolution of 800 nm, there are 5019 large pores with pore diameter smaller than 1 μm, accounting for 1%. Additionally, microfractures of 10 to 15 μm account for 22%, compared with only 6% for other sizes. As can be viewed from Fig. 6a, the large pores with pore

diameter smaller than 1 μm increase significantly when the coal samples CZ is fractured, with the proportion increasing from 1% to 62%. This means that the seepage pores, which show a strong stress sensitivity, are more affected by the compression effect (Ribeiro et al., 2019; Wang et al., 2020c; Zhang et al., 2019b). Aiming at medium-rank coal QY in the original condition, the number of large pores with pore diameter less than 1 μm and super-large pores with pore diameter from 1 to 10 μm is similar in the resolution range, both accounting for about 43%. Therefore, this demonstrates that the QY is more susceptible to methane seepage than CZ in the original condition (Zhao et al., 2022).

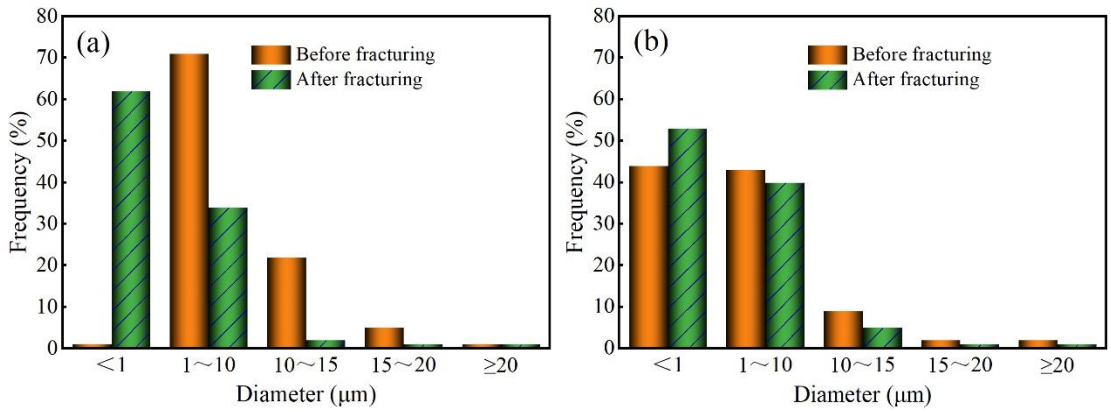

Fig. 6. Histograms of pore-fracture frequency distribution for different scale ranges. (a)-the coal sample CZ; (b)-the coal sample QY.

Regardless of the coal sample CZ or QY, the proportion of large pores with pore diameter less than 1 μm increases significantly after fracturing. It is noteworthy that the variation range of different pore-fracture scales of QY is smaller than that of CZ after fracturing, indicating that the distribution of different ranges of pore-fractures is more uniform in QY than in CZ. Combining the pore-fracture distribution in different ranges with Fig. 2, we can find that the primary and secondary pores of the medium- and high-

rank coals form a complex network of pore-fracture structures for fluid transport through continuous connection and expansion due to compression, which provides powerful conditions for the transformation of methane from laminar to turbulent flow in coal.

4.2.2. Quantitative analysis of pore-throat connectivity

For pore-throat connectivity (PTC), the range of throat length after fracturing of the coal sample CZ shifts from 0.5 and 1.3 μm to 0.5 and 2.5 μm (Fig. 7$a_1$and a_2), and that of the coal sample QY changes from 0.5 and 3.7 μm to 0.5 and 2.5 μm (Fig. 7$b_1$and b_2). Additionally, the proportion of throats from 5 to 10 μm in the original CZ is the highest (about 69%); however, the throats larger than 20 μm increase by 43% after fracturing (Fig. 7a_3), which may be related to the higher ash content in the CZ (Keller et al., 2013; Li et al., 2021b; Yu et al., 2020). The average pore-throat ratio of CZ increases from 1.05% to 4.93% during the whole fracturing process (Fig. 7b_3), which is extremely beneficial to the improvement of PTC. Similarly, QY also has the highest proportion of throats between 5 to 10 μm before fracturing. However, the number of throats less than 5 μm increases by 22% after fracturing, with a particular increase of 6832 throats between 800 to 1000 nm. This indicates that the number of throats with larger lengths is significantly reduced by compression, resulting in a substantial enhancement of PTC (Li et al., 2022; Ribeiro et al., 2016).

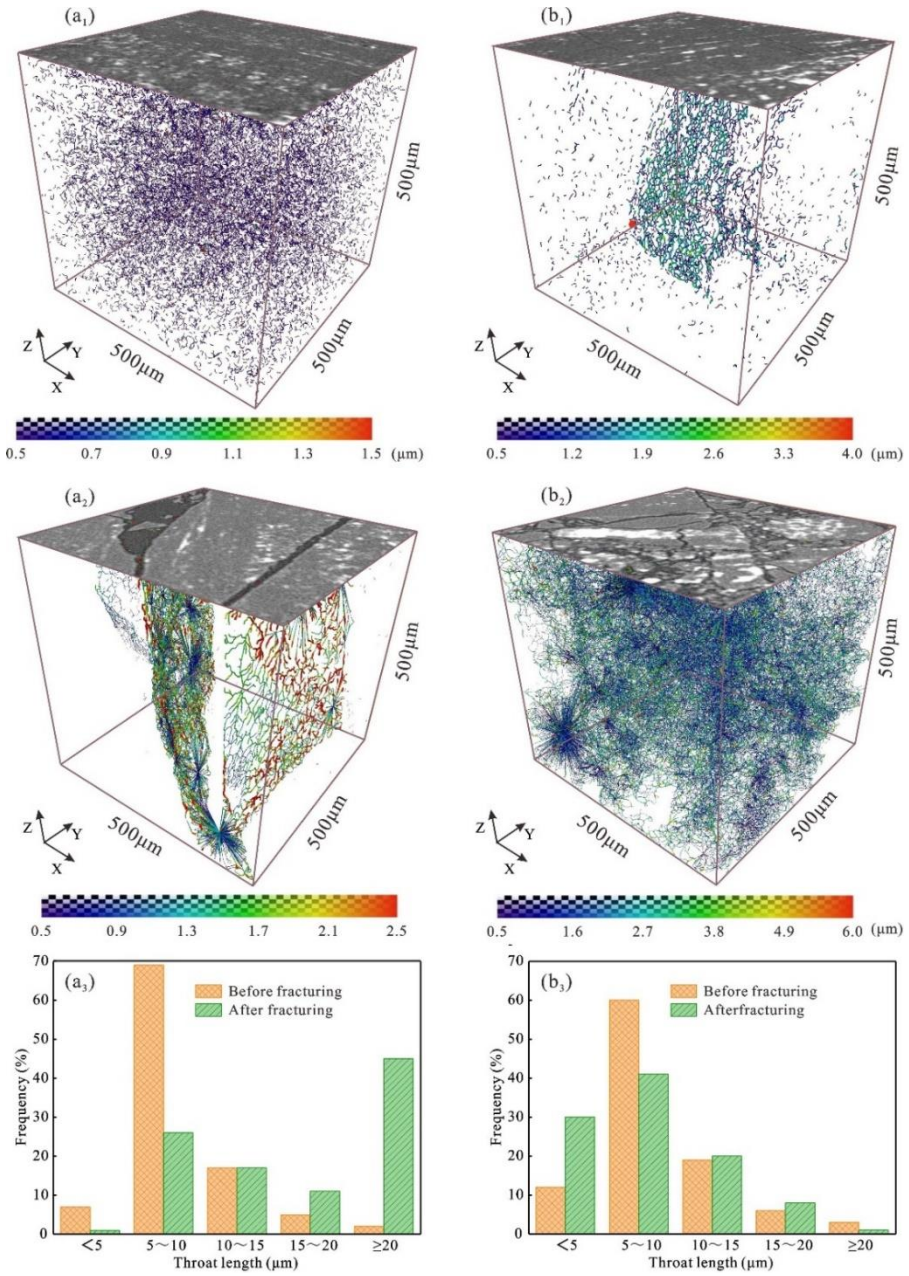

Fig. 7. PTC analysis of coal samples CZ and QY based on nano-CT. a_1 and a_2 indicate the distribution of throat radius of the coal sample CZ before and after fracturing, respectively; b_1 and b_2 represent the distribution of throat radius of the coal sample QY before and after fracturing, respectively. a_3 and b_3 denote the frequency of throat length distribution of 500 × 500 × 500 μm cubes in coal samples CZ and QY, respectively.

4.2.3. Evaluation of stress sensitivity during loading

The stress sensitivity occurring in coal plays an essential role in influencing the production variation during CBM development (Tan et al., 2021; Tan et al., 2019). Generally, the permeability of coal decreases with the increase of effective stress (Shao et al., 2020), especially the stress sensitivity of water-bearing coal cores. At the same rate of effective stress change, the fracture volume deformation of small-scale coal samples is greater than that of large-scale (Jia et al., 2022a), so the stress sensitivity of the former is stronger than that of the latter. For reservoirs with high-stress long-term action, the creep behavior caused by plastic deformation of salt minerals can affect reservoir permeability (Wu et al., 2020), which makes the evaluation of stress sensitivity more complicated. Compared with conventional oil and gas reservoirs, CBM reservoirs exhibit high-stress sensitivity due to low strength and high Poisson's ratio.

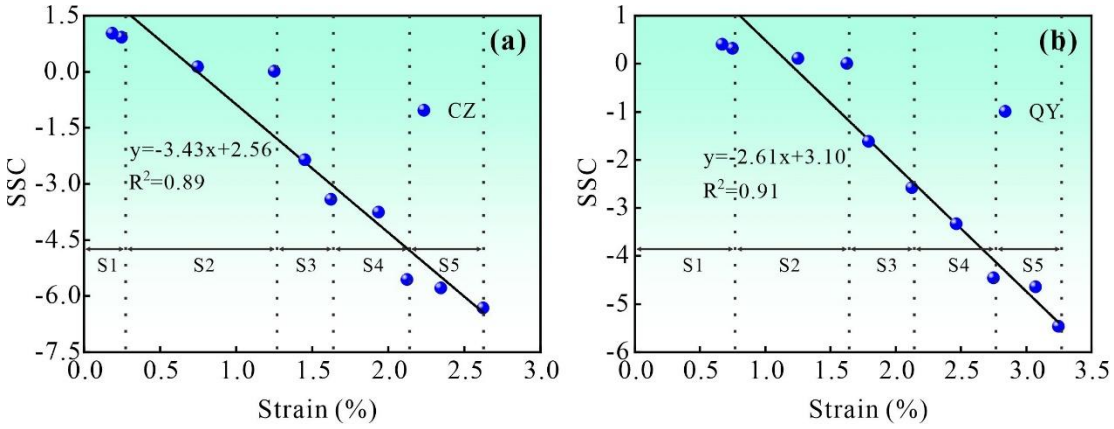

Fig. 8. The stress sensitivity coefficients for different deformation stages during loading.

During the fracturing process, the pore-fracture system changes due to the increasing stress, which changes the permeability of coal sample. To further analyze the pore-fracture sensitivity of medium- and high-rank coals in the whole loading process,

we used the method of Shao et al. (2020) to investigate the stress sensitivity coefficient S_s, which is calculated as Equation (5). It should be noted that S_s between 0.7 and 1 reflect strong stress sensitivity (Shao et al., 2020), while $S_s < 0.05$ indicates no stress sensitivity. As illustrated in Fig. 8, the coal sample CZ exhibits a stress sensitivity coefficient of ~0.91 at the initial compression stage, indicating a strong stress sensitivity, which has a greater impact on the closure of microfractures and the reduction of permeability. When the strain ranges from 0.75% to 1.25%, the stress sensitivity coefficient decreases from 0.13 to 0.02 (Fig. 8a). In other words, the stress sensitivity experiences a change from weak to none, implying that the original microfractures no longer continued to close (Liu et al., 2018). As the strain continues to increase, the stress sensitivity coefficient changes to a negative value, showing that the permeability changes from a decreasing trend to a significant increase. For the coal sample QY, a stress sensitivity coefficient of ~0.32 is displayed in the initial compression stage (Fig. 8b), denoting a relatively weak stress sensitivity. Similarly, the stress sensitivity of QY undergoes a change from weak to none in the linear elastic stage. Subsequently, the stress sensitivity coefficient becomes negative, indicating that a large number of new pore-fractures are generated, which is very beneficial for fluid transport during the drainage process of CBM wells (Cui et al., 2019; Lu et al., 2022b). In conclusion, the stress sensitivity of CZ is stronger than that of QY, and the stress sensitivity coefficients of both coal samples show a decreasing trend during the fracturing process.

$$S_s = \frac{1-(\frac{k_i}{k_0})^{\frac{1}{3}}}{\lg\frac{\sigma_i}{\sigma_0}} \quad (5)$$

where k_0 and σ_0 denote the original permeability and stress at the initial measurement point, respectively; k_i and σ_i represent the permeability and stress of the ith test, respectively.

4.3. 3D fractal dimension variation with computational domain

Coal is a kind of porous material with strong anisotropy, which brings challenges to the fine analysis of pore-fracture networks (Mishra et al., 2018; Wu et al., 2019a; Zhao et al., 2021a). Due to the differences in the complexity of individual sections in the 2D fractal dimension analysis space, the 3D fractal dimension is used to compensate for the shortcomings in the calculation process (Mangi et al., 2020). The 3D fractal dimension (Wu et al., 2019a), indicating the validity of the space occupied by complex forms, is a new branch of modern geometry. In general, the local features (morphology, structure, function or energy, etc.) of an object show similarity to the whole (Shi et al., 2018), which can be reflected by the 3D fractal dimension. Therefore, the 3D fractal dimension may become a measure of the spatial irregularity of complex forms (Li et al., 2021b). CBM is extracted in underground 3D space, and the 3D fractal dimension is commonly used to describe the complexity and self-similar structure of porous media (Wang et al., 2019). Moreover, the heterogeneity of coal reservoirs is also commonly characterized quantitatively by the 3D fractal dimension (Shi et al., 2018; Wang et al., 2022; Zhang et al., 2020). Similar to Wu et al. (2019b), we defined a new cube as a

computational domain for every additional 10 pixels in the cube formed by 1200 CT. From Fig. 9, the 3D fractal dimensions of medium- and high-rank coals show a trend of first increasing and then stabilizing with the increase of the computational domain. This suggests that the fractal dimension of the 3D space of coal samples should be as large as possible to reduce the calculation error. It is worth noting that the side length of the computational domain of the two coal samples in the original state before reaching the stable value is linearly related to the 3D fractal dimension, while the computational domain size after fracturing is logarithmically correlated with the 3D fractal dimension. Moreover, there are many mutation points in the 3D fractal dimension of coal samples after fracturing, mainly due to the generation of new pore-fractures at different locations of the computational domain. With the increase of the computational domain side length, the 3D fractal dimension of the fractured coal sample reaches a stable value slightly later than that in the original state, which is attributed to the enhanced irregularity and heterogeneity of the pore-fracture in the coal (Liu et al., 2021a).

As depicted in Fig. 9a and b, the CZ in the original state exhibits a 3D fractal dimension of 2.42 after stabilization, while the fractal dimension after fracturing reaches 2.72. This confirms the previous analysis that the pore-fracture becomes more developed and the connection between seepage pore and microfracture is also more complicated. The 3D fractal dimension of QY increases by 0.29 after fracturing (Fig. 9c and d), which significantly improves the fluid transport efficiency of the whole coal sample. It should be noted that the 3D fractal dimension of QY is always higher than

that of CZ, indicating that the fluid pressure propagation of QY may reach equilibrium more easily.

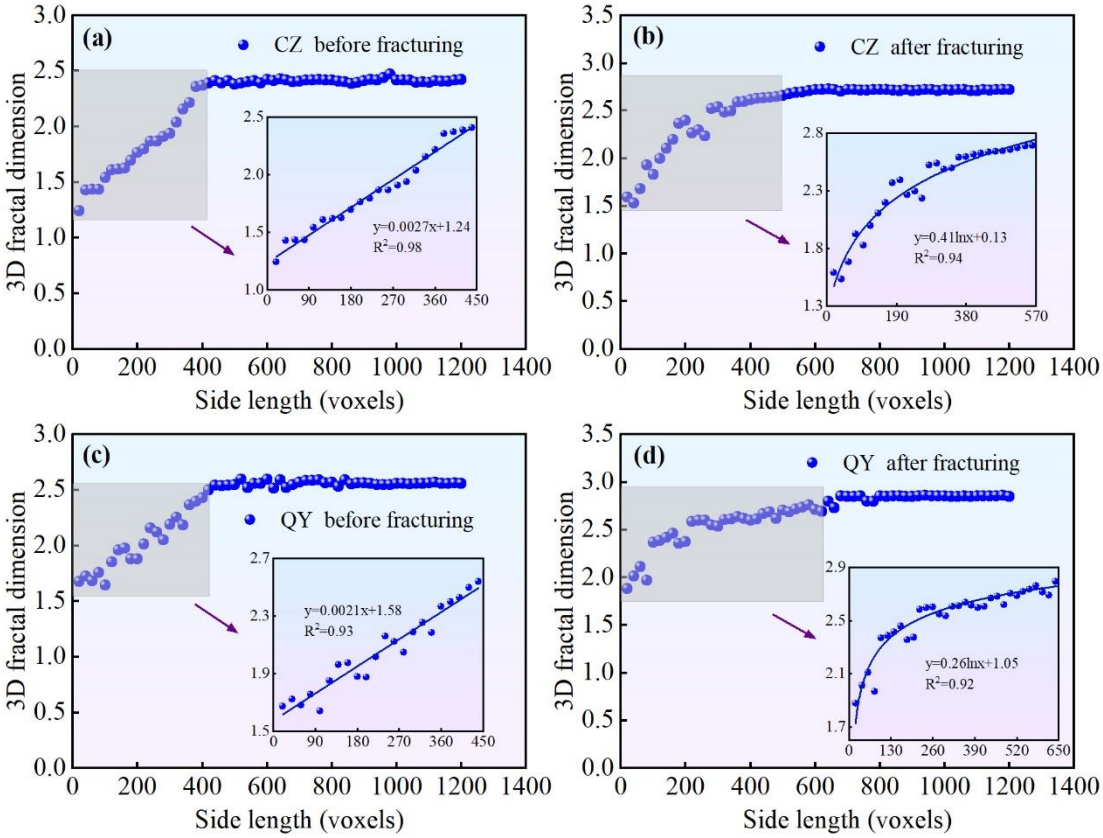

Fig. 9. The relationship between different computational domain sizes and 3D fractal dimension for medium- and high-rank coals.

4.4. Changes in diffusion transport caused by loading

4.4.1. Heterogeneous distribution of fluid pressure

As a measure of fluid energy in coal reservoirs, fluid pressure plays an essential role in controlling gas content and fluid phase (Hou et al., 2022; Yan et al., 2017). The initial inlet pressure of 2.5 MPa was set for the simulation based on the change of bottom-hole flow pressure propagation in the process of CBM drainage. The coal sample CZ has relatively few connection pores in the original state (Fig. 5), causing the fluid transport

resistance to be larger than that of the coal sample QY. From Fig. 10, it can be found that the fluid pressure of QY after fracturing spreads in a wider range than CZ, accompanied by more distribution of high fluid pressure. In the simulation process, the narrow and long throat with a low coordination number is the main inducer of fluid pressure mutation. The presence of red and blue spheres in both CZ and QY indicates the existence of narrow and long throats with low coordination numbers here (Fig. 10a_1, a_3, b_1 and b_2). Most of the fluid pressure in the Y direction of CZ is concentrated between 0.1 and 0.3 MPa (Fig. 11a_2), suggesting that the capillary resistance in this direction is higher (Melnichenko et al., 2009; Zhang et al., 2019a). Moreover, the fluid pressure distributions in the X and Z directions are more dispersed, ranging from 0.4 to 2.5 MPa and 0.3 to 2.5 MPa (Fig. 11a_1 and a_3), respectively, implying that the anisotropy in these two directions is stronger than that in the Y direction. For the coal sample QY, the fluid pressure in the X and Y directions mainly ranges from 0.2 to 1.3 MPa and 1.8 to 2.45 MPa, respectively (Fig. 11b_1 and b_3), indicating the difference in diffusion resistance of QY in different directions. It is worth noting that the number of connection pores in QY is much larger than that in CZ, demonstrating that CZ requires a greater energy drive to induce fluid transport.

As shown in Fig. 12, there are differences in the frequency of fluid pressure distribution in X, Y and Z directions, which are mainly caused by the anisotropy and heterogeneity of different microstructures. The distribution of fluid pressure less than 0.5 MPa in the Y direction of the coal sample CZ is close to 100%, exhibiting a more concentrated distribution than in the X and Y directions (Fig. 12a). Due to the relatively

developed QY pore-fracture of the fractured coal samples, the fluid pressure distributions of X, Y and Z are not much different, and the pressure distributions in different ranges are all below 50% (Fig. 12b). Therefore, the coal sample QY generally reaches fluid pressure equilibrium quicker than CZ, which is beneficial for the drainage in the actual development of CBM (Xie et al., 2020).

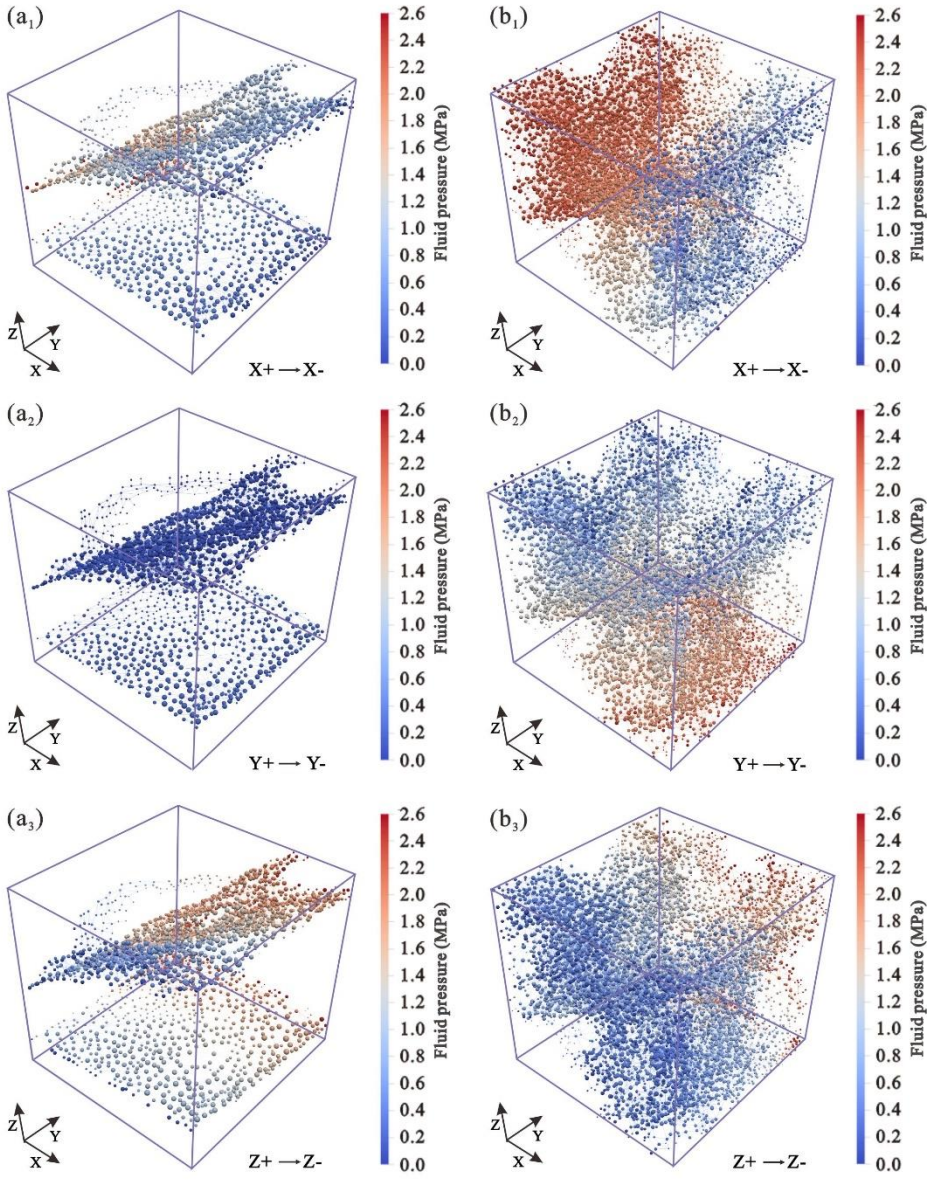

Fig. 10. The 3D propagation changes of fluid pressure in different directions after fracturing. a_1, a_2 and a_3 represent the fluid pressure propagation in X, Y, and Z directions for the coal sample CZ, respectively. b_1, b_2 and b_3 indicate the fluid pressure propagation in X, Y, and Z directions for the

coal sample QY, respectively. The initial inlet pressure of 2.5 MPa was set for the simulation based on the change of bottom-hole flow pressure propagation in the process of CBM drainage.

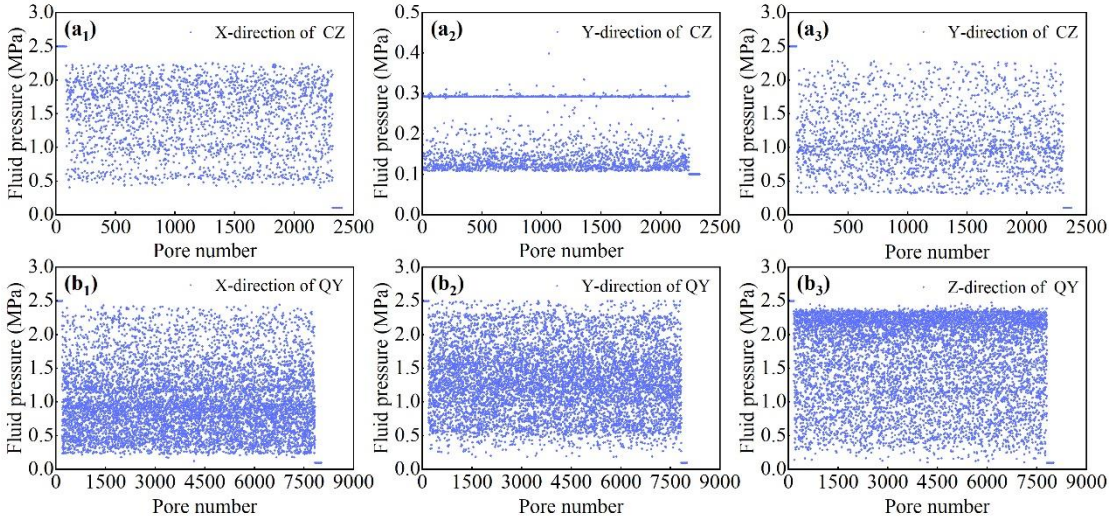

Fig. 11. Fluid pressure distribution of different coal samples.

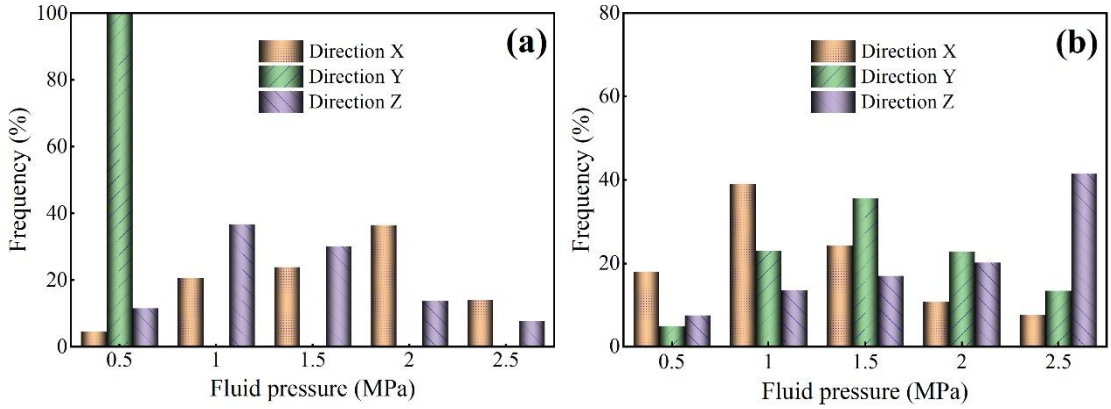

Fig. 12. Frequency distribution of different ranges of fluid pressure. (a)-the coal sample CZ; (b)-the coal sample QY.

4.4.2. Diffusion effect of gas transport

As presented in Fig. 13, the diffusion coefficient of methane in coal at constant temperature increases logarithmically with increasing gas injection pressure for both coal samples CZ and QY. Comparing Fig. 13a and b, the increase of diffusion coefficient of QY is larger than that of CZ, indicating that the diffusion ability of the

medium-rank coal is stronger than that of high-rank coal with the increase of gas injection pressure. Under the gas pressure condition of 0.5 MPa, the diffusion coefficient of fractured CZ is 350 times higher than that in the original condition, and the QY increases 414 times than its original, indicating that fracturing provides favorable conditions for fluid propagation in diffusion and seepage pores (Li et al., 2016; O'Neill et al., 2021). Obviously, the gas resistance of medium- and high-rank coals after fracturing is significantly reduced, which provides the possibility for more gas to be converted from Knudsen diffusion to transition diffusion or Fick diffusion in the channel (Li et al., 2020c; Zhao et al., 2017). At the same time, the effects of velocity sensitivity, water sensitivity and water lock between fluid and solid are attenuated due to the expansion and penetration of fluid channels (Li et al., 2020b; Liu et al., 2021b). Additionally, the diffusion coefficient of the fractured QY under the gas pressure condition of 5 MPa is 3.4 times higher than that of CZ, demonstrating that the connection effect between pores and microfractures after fracturing QY is noticeably better than that of the CZ. Therefore, in the fractured medium-rank coal QY, it is easier for fluid to propagate among diffusion pores, seepage pores and microfractures than in the high-rank coal CZ.

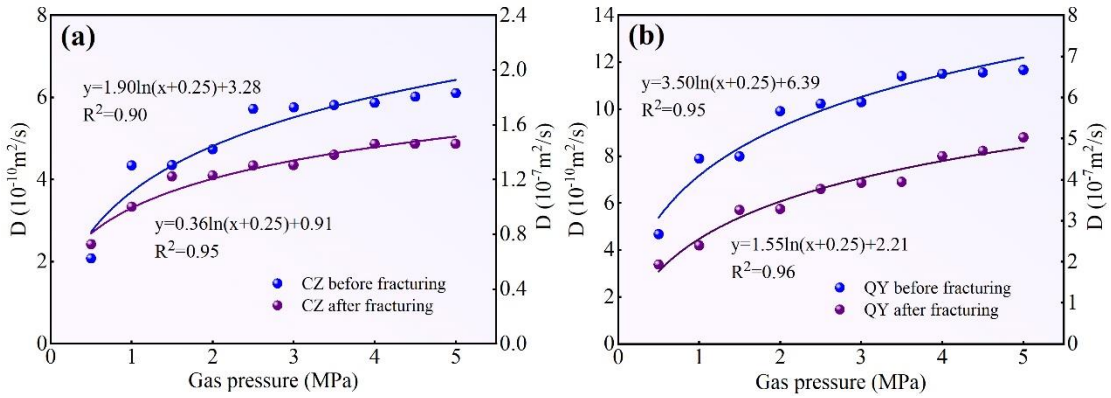

Fig. 13. Variation of the diffusion coefficient of medium- and high-rank coals under different gas pressure.

5. Conclusions

In this work, the deformation characteristics and dynamic evolution of the pore-fracture system of fractured medium- and high-rank coals were investigated by Nano-CT, followed by the evaluation of stress sensitivity, 3D fractal characteristics and heterogeneous distribution of fluid pressure. Subsequently, changes in diffusion effects of gas transport induced by fracturing were characterized. The following conclusions are drawn:

(1) With increased axial stress, the pore-fractures of both medium- and high-rank coals undergo damage phenomena of compaction, growth, and penetration. The strain of CZ in the linear elastic stage increases from 0.25% to 1.25%, greater than that of QY from 0.75% to 1.63%, demonstrating a slight lag of the high-rank coal from the linear elastic stage into the yielding stage.

(2) Regardless of the coal sample CZ or QY, the proportion of large pores with pore diameter less than 1 μm increases significantly after fracturing. It is noteworthy that the variation range of different pore-fracture scales of QY is smaller than that of CZ, indicating that the distribution of different ranges of pore-fractures in QY is relatively uniform. In the original state, the highest percentage of 5 to 10 μm throat is found in QY. However, the number of throats less than 5 μm increases by 22% after fracturing, with a particular increase of 6832 throats between 800 to 1000 nm.

(3) The 3D fractal dimension of both medium- and high-rank coals shows a trend of

first increasing and then stabilizing as the computational domain increases. Moreover, there are many mutation points in the 3D fractal dimension of coal samples after fracturing, mainly due to the generation of new pore-fractures at different locations of the computational domain.

(4) Due to the relatively developed pore-fracture in QY after fracturing, the fluid pressure distributions in X, Y and Z directions are not much different. Therefore, QY is generally easier to achieve the equilibrium of fluid pressure system than CZ. The diffusion coefficient of the fractured QY is 414 times higher than that of the original coal under the gas pressure condition of 0.5 MPa, which enhances the efficiency of fluid propagation in the diffusion and seepage pores.

CRediT authorship contribution statement

Qifeng Jia: Writing - original draft, Investigation, Methodology, Data curation. **Dameng Liu**: Supervision, Conceptualization, Methodology, Funding acquisition, Writing - review & editing. **Yidong Cai**: Supervision, Funding acquisition, Writing - review & editing. **Yuejian Lu**: Writing - review & editing, Software. **Rui Li**: Methodology, Image Processing. **Hao Wu**: Image Processing, Software. **Yingfang Zhou**: Supervision, Writing - review & editing.

Declaration of Competing interests

The authors declare that they have no known competing financial interests or personal relationships that could have appeared to influence the work reported in this paper.

Acknowledgements

This research was funded by the National Natural Science Foundation of China (grant nos. 42130806, 41830427and 41922016), 2021 Graduate Innovation Fund Project of China University of Geosciences, Beijing (grant no. ZD2021YC035) and the Fundamental Research Funds for Central Universities (grant no. 2-9-2021-067). We are very grateful to the reviewers and editors for their valuable comments and suggestions.

Nomenclature

i Number of pores connected at the beginning of the throat

j Number of pores connected at the end of the throat

Q Flow rate [m^3/s]

K Hydraulic conduction coefficient

P_i The pressure of the ith pore [MPa]

P_j The pressure of the jth pore [MPa]

μ The dynamic viscosity of the liquid [Pa·s]

l The length of the throat [μm]

r The radius of the throat [μm]

D Diffusion coefficient [m^2/s]

S The cross-sectional area of coal sample [m^2]

L The height of coal sample [m]

t Diffusion time [s]

V' The volumes of gas chambers 1 [m^3]

V'' The volumes of gas chambers 2 [m^3]

S_s Stress sensitivity coefficient

k_0 Original permeability [mD]

σ_0 The stress at the initial measurement point [MPa]

k_i The permeability of the ith test [mD]

σ_i The stress of the ith test [MPa]

References

Akhondzadeh, H., Keshavarz, A., Al-Yaseri, A.Z., Ali, M., Awan, F.U.R., Wang, X., Yang, Y., Iglauer, S., Lebedev, M., 2020. Pore-scale analysis of coal cleat network evolution through liquid nitrogen treatment: A Micro-Computed Tomography investigation. Int. J. Coal Geol. 219, 103370.

Cai, Y., Liu, D., Pan, Z., Yao, Y., Li, J., Qiu, Y., 2013. Pore structure and its impact on CH_4 adsorption capacity and flow capability of bituminous and subbituminous coals from Northeast China. Fuel 103, 258-268.

Chen, J., Cheng, W., Wang, G., 2021a. Simulation of the meso-macro-scale fracture network development law of coal water injection based on a SEM reconstruction fracture COHESIVE model. Fuel 287, 119475.

Chen, Y., Ma, D., Guo, C., Yang, F., Mu, T., Gao, Z., 2019. An Experimental Study on the Conductivity Changes in Coal during Methane Adsorption-Desorption and their Influencing Factors. Acta Geol. Sin. - Engl. 93, 704-717.

Chen, Y., Ma, Z., Ma, D., Zhang, Z., Li, W., Yang, F., Ji, Y., Peng, T., Meng, Y., 2021b. Characteristics of the Coal Fines Produced from Low-Rank Coal Reservoirs and Their Wettability and Settleability in the Binchang Area, South Ordos Basin, China. Geofluids 2021, 1-17.

Connell, L.D., 2009. Coupled flow and geomechanical processes during gas production from coal

seams. Int. J. Coal Geol. 79, 18-28.

Cui, J., Liu, D., Cai, Y., Pan, Z., Zhou, Y., 2019. Insights into fractures and minerals in subbituminous and bituminous coals by FESEM-EDS and X-ray μ-CT. Fuel 237, 977-988.

Dai, S., Bechtel, A., Eble, C.F., Flores, R.M., French, D., Graham, I.T., Hood, M.M., Hower, J.C., Korasidis, V.A., Moore, T.A., Püttmann, W., Wei, Q., Zhao, L., O'Keefe, J.M.K., 2020a. Recognition of peat depositional environments in coal: A review. Int. J. Coal Geol. 219, 103383.

Dai, S., Finkelman, R.B., French, D., Hower, J.C., Graham, I.T., Zhao, F., 2021. Modes of occurrence of elements in coal: A critical evaluation. Earth-Sci. Rev. 222, 103815.

Dai, S., Hower, J.C., Finkelman, R.B., Graham, I.T., French, D., Ward, C.R., Eskenazy, G., Wei, Q., Zhao, L., 2020b. Organic associations of non-mineral elements in coal: A review. Int. J. Coal Geol. 218, 103347.

Deschamps, R., Sale, S.O., Chauveau, B., Fierens, R., Euzen, T., 2017. The coal-bearing strata of the Lower Cretaceous Mannville Group (Western Canadian Sedimentary Basin, South Central Alberta). Part 1: Stratigraphic architecture and coal distribution controlling factors. Int. J. Coal Geol. 179, 113-129.

Du, Z., Huang, Q., Guo, J., Gao, F., Du, Y., 2020. The occurrence of nano- and micro-scale pores and their controls on the selective migration of gases in the coals of different ranks. Fuel 264, 116748.

Duan, M., Jiang, C., Yin, W., Yang, K., Li, J., Liu, Q., 2021. Experimental study on mechanical and damage characteristics of coal under true triaxial cyclic disturbance. Eng. Geol. 295, 106445.

Fu, X., Zhao, C., Lun, Z., Wang, H., Wang, M., Zhang, D., 2021. Influences of controlled microwave field radiation on pore structure, surface chemistry and adsorption capability of gas-bearing shales. Mar. Petrol. Geol. 130, 105134.

Hou, Y., Peng, Y., Chen, Z., Liu, Y., Tian, Y., 2022. Investigating heterogeneous distribution of fluid pressure in hydraulic fractures during pulsating hydraulic fracturing. J. Petrol. Sci. Eng. 209, 109823.

Jia, Q., Liu, D., Cai, Y., Fang, X., Li, L., 2020. Petrophysics characteristics of coalbed methane reservoir: A comprehensive review. Front. Earth Sci. 15, 202-223.

Jia, Q., Liu, D., Cai, Y., Zhou, Y., Zhao, Z., Yang, Y., 2022a. AFM characterization of physical properties in coal adsorbed with different cations induced by electric pulse fracturing. Fuel 327, 125247.

Jia, Q., Liu, D., Ni, X., Cai, Y., Lu, Y., Li, Z., Zhou, Y., 2022b. Interference mechanism in coalbed methane wells and impacts on infill adjustment for existing well patterns. Energy Rep. 8, 8675-8689.

Ju, Y., Xi, C., Wang, S., Mao, L., Wang, K., Zhou, H., 2021. 3-D fracture evolution and water migration in fractured coal under variable stresses induced by fluidized mining: In situ triaxial loading and CT imaging analysis. Energy Rep. 7, 3060-3073.

Kang, J., Elsworth, D., Fu, X., Liang, S., Chen, H., 2022. Contribution of thermal expansion on gas adsorption to coal sorption-induced swelling. Chem. Eng. J. 432, 134427.

Kang, J., Fu, X., Li, X., Liang, S., 2019. Nitrogen injection to enhance methane and water production: An experimental study using the LF-NMR relaxation method. Int. J. Coal Geol. 211, 103228.

Keller, L.M., Schuetz, P., Erni, R., Rossell, M.D., Lucas, F., Gasser, P., Holzer, L., 2013. Characterization of multi-scale microstructural features in Opalinus Clay. Micropor. Mesopor. Mat. 170, 83-94.

Li, J., Huang, Q., Wang, G., Wang, E., Ju, S., Qin, C., 2022. Experimental study of effect of slickwater fracturing on coal pore structure and methane adsorption. Energy 239, 122421.

Li, Q., Liu, D., Cai, Y., Zhao, B., Lu, Y., Zhou, Y., 2021a. Effects of natural micro-fracture morphology, temperature and pressure on fluid flow in coals through fractal theory combined with lattice Boltzmann method. Fuel 286, 119468.

Li, Q., Liu, D., Cai, Y., Zhou, Y., Yin, T., 2021b. Investigation on the Methane Adsorption Capacity in Coals: Considerations from Nanopores by Multifractal Analysis. Energ. Fuel. 35, 6633-6643.

Li, Y., Cui, H., Zhang, P., Wang, D., Wei, J., 2020a. Three-dimensional visualization and quantitative characterization of coal fracture dynamic evolution under uniaxial and triaxial compression based on μCT scanning. Fuel 262, 116568.

Li, Y., Wang, Y., Wang, J., Pan, Z., 2020b. Variation in permeability during CO_2–CH_4 displacement in coal seams: Part 1 – Experimental insights. Fuel 263, 116666.

Li, Y., Xu, W., Wu, P., Meng, S., 2020c. Dissolution versus cementation and its role in determining tight sandstone quality: A case study from the Upper Paleozoic in northeastern Ordos Basin, China. J. Nat. Gas Sci. Eng. 78, 103324.

Li, Y., Yang, J., Pan, Z., Tong, W., 2020d. Nanoscale pore structure and mechanical property analysis of coal: An insight combining AFM and SEM images. Fuel 260.

Li, Z., Liu, D., Cai, Y., Shi, Y., 2016. Investigation of methane diffusion in low-rank coals by a multiporous diffusion model. J. Nat. Gas Sci. Eng. 33, 97-107.

Liu, A., Liu, P., Liu, S., 2020. Gas diffusion coefficient estimation of coal: A dimensionless numerical method and its experimental validation. Int. J. Heat Mass Tran. 162, 120336.

Liu, D., Yao, Y., Chang, Y., 2022a. Measurement of adsorption phase densities with respect to different pressure: Potential application for determination of free and adsorbed methane in coalbed methane reservoir. Chem. Eng. J. 446, 137103.

Liu, D., Yao, Y., Wang, H., 2022b. Structural compartmentalization and its relationships with gas accumulation and gas production in the Zhengzhuang Field, southern Qinshui Basin. Int. J. Coal Geol. 259, 104055.

Liu, D., Zou, Z., Cai, Y., Qiu, Y., Zhou, Y., He, S., 2021a. An updated study on CH4 isothermal adsorption and isosteric adsorption heat behaviors of variable rank coals. J. Nat. Gas Sci. Eng. 89, 103899.

Liu, Q., Wang, J., Liu, J., Yang, Q., Huang, W., Liu, Y., Wang, L., 2022c. Determining diffusion coefficients of coal particles by solving the inverse problem based on the data of methane desorption measurements. Fuel 308, 122045.

Liu, Y., Yu, P., Ding, Z., 2018. Research on stress-sensitivity of fractured porous media. J. Petrol. Sci. Eng. 171, 879-889.

Liu, Z., Liu, D., Cai, Y., Qiu, Y., 2021b. Permeability, mineral and pore characteristics of coals response to acid treatment by NMR and QEMSCAN: Insights into acid sensitivity mechanism. J. Petrol. Sci. Eng. 198, 108205.

Lu, Y., Liu, D., Cai, Y., Gao, C., Jia, Q., Zhou, Y., 2022a. AFM measurement of roughness, adhesive force and wettability in various rank coal samples from Qinshui and Junggar basin, China. Fuel 317, 123556.

Lu, Y., Liu, D., Cai, Y., Li, Q., Zhou, Y., 2022b. Spontaneous imbibition in coal with in-situ dynamic micro-CT imaging. J. Petrol. Sci. Eng. 208, 109296.

Lu, Y., Wang, L., Ge, Z., Zhou, Z., Deng, K., Zuo, S., 2020. Fracture and pore structure dynamic evolution of coals during hydraulic fracturing. Fuel 259, 116272.

Mangi, H.N., Detian, Y., Hameed, N., Ashraf, U., Rajper, R.H., 2020. Pore structure characteristics

and fractal dimension analysis of low rank coal in the Lower Indus Basin, SE Pakistan. J. Nat. Gas Sci. Eng. 77, 103231.

Melnichenko, Y.B., Radlinski, A.P., Mastalerz, M., Cheng, G., Rupp, J., 2009. Characterization of the CO2 fluid adsorption in coal as a function of pressure using neutron scattering techniques (SANS and USANS). Int. J. Coal Geol. 77, 69-79.

Mishra, D.K., Samad, S.K., Varma, A.K., Mendhe, V.A., 2018. Pore geometrical complexity and fractal facets of Permian shales and coals from Auranga Basin, Jharkhand, India. J. Nat. Gas Sci. Eng. 52, 25-43.

O'Neill, K.T., Birt, B., Hopper, T., 2021. Borehole measurements of adsorbed gas content in coals using stimulated diffusion nuclear magnetic resonance. Int. J. Coal Geol. 247, 103845.

Qin, X., Cai, J., Zhou, Y., Kang, Z., 2020. Lattice Boltzmann simulation and fractal analysis of effective thermal conductivity in porous media. Appl. Therm. Eng. 180, 115562.

Ribeiro, J., Machado, G., Moreira, N., Suárez-Ruiz, I., Flores, D., 2019. Petrographic and geochemical characterization of coal from Santa Susana Basin, Portugal. Int. J. Coal Geol. 203, 36-51.

Ribeiro, J., Suárez-Ruiz, I., Flores, D., 2022. Coal related fires in Portugal: New occurrences and new insights on the characterization of thermally affected and non-affected coal waste piles. Int. J. Coal Geol. 252, 103941.

Ribeiro, J., Suárez-Ruiz, I., Ward, C.R., Flores, D., 2016. Petrography and mineralogy of self-burning coal wastes from anthracite mining in the El Bierzo Coalfield (NW Spain). Int. J. Coal Geol. 154-155, 92-106.

Roslin, A., Pokrajac, D., Wu, K., Zhou, Y., 2020. 3D pore system reconstruction using nano-scale

2D SEM images and pore size distribution analysis for intermediate rank coal matrix. Fuel 275, 117934.

Shao, J., You, L., Kang, Y., Gao, X., Chen, M., Meng, S., Zhang, N., 2020. Experimental study on stress sensitivity of underground gas storage. J. Petrol. Sci. Eng. 195, 107577.

Shi, X., Pan, J., Hou, Q., Jin, Y., Wang, Z., Niu, Q., Li, M., 2018. Micrometer-scale fractures in coal related to coal rank based on micro-CT scanning and fractal theory. Fuel 212, 162-172.

Shi, X., Pan, J., Pang, L., Wang, R., Li, G., Tian, J., Wang, H., 2020. 3D microfracture network and seepage characteristics of low-volatility bituminous coal based on nano-CT. J. Nat. Gas Sci. Eng. 83, 103556.

Song, H., Lin, B., Zhong, Z., Liu, T., 2022. Experimental study on methane diffusion kinetics in three typical metamorphic coals. Fuel 311, 122601.

Tamamura, S., Murakami, T., Ueno, A., Tamazawa, S., Kiyama, T., Inomata, H., Matsumoto, H., Uchida, K., Suzuki, Y., Aizawa, J., Kaneko, K., 2020. Formation of coalbed methane and water-dissolved gas in Kushiro Coal Mine, Japan, based on isotopic compositions of gas, groundwater, and calcite. Int. J. Coal Geol. 229, 103577.

Tan, Q., Kang, Y., You, L., Xu, C., Zhang, X., Xie, Z., 2021. Stress-sensitivity mechanisms and its controlling factors of saline-lacustrine fractured tight carbonate reservoir. J. Nat. Gas Sci. Eng. 88, 103864.

Tan, Y., Pan, Z., Feng, X.-T., Zhang, D., Connell, L.D., Li, S., 2019. Laboratory characterisation of fracture compressibility for coal and shale gas reservoir rocks: A review. Int. J. Coal Geol. 204, 1-17.

Tao, M., Jl, X., Xm, L., Jw, M., Yang, Y., 2020. Experimental study on the evolutional trend of pore

structures and fractal dimension of low-rank coal rich clay subjected to a coupled thermo-hydro-mechanical-chemical environment. Energy 203, 117838.

Wang, C., Liu, J., Feng, J., Wei, M., Wang, C., Jiang, Y., 2016. Effects of gas diffusion from fractures to coal matrix on the evolution of coal strains: Experimental observations. Int. J. Coal Geol. 162, 74-84.

Wang, D., Zeng, F., Wei, J., Zhang, H., Wu, Y., Wei, Q., 2021a. Quantitative analysis of fracture dynamic evolution in coal subjected to uniaxial and triaxial compression loads based on industrial CT and fractal theory. J. Petrol. Sci. Eng. 196, 108051.

Wang, D., Zhang, P., Wei, J., Yu, C., 2020a. The seepage properties and permeability enhancement mechanism in coal under temperature shocks during unloading confining pressures. J. Nat. Gas Sci. Eng. 77, 103242.

Wang, G., Han, D., Qin, X., Liu, Z., Liu, J., 2020b. A comprehensive method for studying pore structure and seepage characteristics of coal mass based on 3D CT reconstruction and NMR. Fuel 281, 118735.

Wang, G., Qin, X., Shen, J., Zhang, Z., Han, D., Jiang, C., 2019. Quantitative analysis of microscopic structure and gas seepage characteristics of low-rank coal based on CT three-dimensional reconstruction of CT images and fractal theory. Fuel 256, 115900.

Wang, H., Yang, X., Du, F., Wang, G., Wang, Y., Zhao, W., Wang, H., 2021b. Calculation of the diffusion coefficient of gas diffusion in coal: The comparison of numerical model and traditional analytical model. J. Petrol. Sci. Eng. 205, 108931.

Wang, X., Dang, Z., Hou, S., Yuan, Y., Wang, X., Pan, S., 2022. Fractal characteristics of pulverized high volatile bituminous coals with different particle size using gas adsorption. Fuel 315, 122814.

Wang, X., Pan, J., Wang, K., Ge, T., Wei, J., Wu, W., 2020c. Characterizing the shape, size, and distribution heterogeneity of pore-fractures in high rank coal based on X-ray CT image analysis and mercury intrusion porosimetry. Fuel 282, 118754.

Wu, H., Yao, Y., Zhou, Y., Qiu, F., 2019a. Analyses of representative elementary volume for coal using X-ray μ-CT and FIB-SEM and its application in permeability predication model. Fuel 254, 115563.

Wu, H., Zhou, Y., Yao, Y., Wu, K., 2019b. Imaged based fractal characterization of micro-fracture structure in coal. Fuel 239, 53-62.

Wu, T., Pan, Z., Connell, L.D., Camilleri, M., Fu, X., 2020. Apparent gas permeability behaviour in the near critical region for real gases. J. Nat. Gas Sci. Eng. 77, 103245.

Xie, J., Gao, M., Zhang, R., Liu, J., Lu, T., Wang, M., 2020. Gas flow characteristics of coal samples with different levels of fracture network complexity under triaxial loading and unloading conditions. J. Petrol. Sci. Eng. 195, 107606.

Xie, L., You, Q., Wang, E., Li, T., Song, Y., 2022. Quantitative characterization of pore size and structural features in ultra-low permeability reservoirs based on X-ray computed tomography. J. Petrol. Sci. Eng. 208, 109733.

Xu, H., Tang, D., Zhao, J., Li, S., Tao, S., 2015. A new laboratory method for accurate measurement of the methane diffusion coefficient and its influencing factors in the coal matrix. Fuel 158, 239-247.

Xu, Y., Lun, Z., Pan, Z., Wang, H., Zhou, X., Zhao, C., Zhang, D., 2022. Occurrence space and state of shale oil: A review. J. Petrol. Sci. Eng. 211, 110183.

Yan, S., Bi, J., Qu, X., 2017. The behavior of catalysts in hydrogasification of sub-bituminous coal

in pressured fluidized bed. Appl. Energ. 206, 401-412.

Yu, S., Bo, J., Ming, L., Chenliang, H., Shaochun, X., 2020. A review on pore-fractures in tectonically deformed coals. Fuel 278, 118248.

Zhang, D., Li, C., Zhang, J., Lun, Z., Jia, S., Luo, C., Jiang, W., 2019a. Influences of dynamic entrainer-blended supercritical CO_2 fluid exposure on high-pressure methane adsorption on coals. J. Nat. Gas Sci. Eng. 66, 180-191.

Zhang, J., Wei, C., Ju, W., Yan, G., Lu, G., Hou, X., Kai, Z., 2019b. Stress sensitivity characterization and heterogeneous variation of the pore-fracture system in middle-high rank coals reservoir based on NMR experiments. Fuel 238, 331-344.

Zhang, K., Wang, S., Wang, L., Cheng, Y., Li, W., Han, X., Liu, C., Su, H., 2022. 3D visualization of tectonic coal microstructure and quantitative characterization on topological connectivity of pore-fracture networks by Micro-CT. J. Petrol. Sci. Eng. 208, 109675.

Zhang, X., Lin, B., Li, Y., Zhu, C., Li, Q., 2020. Analysis of fractal dimension of coal subjected to electrical breakdown based on nuclear magnetic resonance. J. Nat. Gas Sci. Eng. 79, 103345.

Zhang, X., Zhu, Z., Wen, G., Lang, L., Wang, M., 2021. Study on gas desorption and diffusion kinetic behavior in coal matrix using a modified shrinking core model. J. Petrol. Sci. Eng. 204, 108701.

Zhao, P., Zhuo, R., Li, S., Shu, C.-M., Jia, Y., Lin, H., Chang, Z., Ho, C.-H., Laiwang, B., Xiao, P., 2021a. Fractal characteristics of methane migration channels in inclined coal seams. Energy 225, 120127.

Zhao, W.-B., Hu, S.-Y., Deng, X.-Q., Bai, B., Tao, S.-Z., Sun, B., Wang, Q.-R., Cheng, D.-X., 2021b. Physical property and hydrocarbon enrichment characteristics of tight oil reservoir in Chang 7

division of Yanchang Formation, Xin'anbian oilfield, Ordos Basin, China. Petrol. Sci. 18, 1294-1304.

Zhao, W., Cheng, Y., Jiang, H., Wang, H., Li, W., 2017. Modeling and experiments for transient diffusion coefficients in the desorption of methane through coal powders. Int. J. Heat Mass Tran. 110, 845-854.

Zhao, Y., Lin, B., Liu, T., Zheng, Y., Sun, Y., Zhang, G., Li, Q., 2021c. Multifractal analysis of coal pore structure based on NMR experiment: A new method for predicting T_2 cutoff value. Fuel 283, 119338.

Zhao, Y., Sun, Y., Liu, S., Chen, Z., Yuan, L., 2018. Pore structure characterization of coal by synchrotron radiation nano-CT. Fuel 215, 102-110.

Zhao, Y., Wang, C., Ning, L., Zhao, H., Bi, J., 2022. Pore and fracture development in coal under stress conditions based on nuclear magnetic resonance and fractal theory. Fuel 309, 122112.

Zheng, S., Yao, Y., Liu, D., Cai, Y., Liu, Y., 2018. Characterizations of full-scale pore size distribution, porosity and permeability of coals: A novel methodology by nuclear magnetic resonance and fractal analysis theory. Int. J. Coal Geol. 196, 148-158.

Zheng, S., Yao, Y., Liu, D., Cai, Y., Liu, Y., Li, X., 2019. Nuclear magnetic resonance T2 cutoffs of coals: A novel method by multifractal analysis theory. Fuel 241, 715-724.

Zhou, H.W., Zhong, J.C., Ren, W.G., Wang, X.Y., Yi, H.Y., 2018. Characterization of pore-fracture networks and their evolution at various measurement scales in coal samples using X-ray μCT and a fractal method. Int. J. Coal Geol. 189, 35-49.

Zhou, S., Yan, D., Tang, J., Pan, Z., 2020. Abrupt change of pore system in lacustrine shales at oil- and gas-maturity during catagenesis. Int. J. Coal Geol. 228, 103557.